


**Ultrafast intermode parametric scattering dynamics in room-temperature polariton condensates**Ziyu Ye,<sup>1,\*</sup> Fei Chen,<sup>1,\*</sup> Hang Zhou,<sup>2</sup> Song Luo,<sup>2</sup> Zhenrong Sun,<sup>1</sup> Huailiang Xu,<sup>1</sup> Hongxing Xu,<sup>1</sup> Hui Li <sup>1,†</sup>, Zhanghai Chen,<sup>2,‡</sup> and Jian Wu<sup>1,3,4,5,§</sup><sup>1</sup>*State Key Laboratory of Precision Spectroscopy, East China Normal University, Shanghai 200241, China*<sup>2</sup>*Department of Physics, College of Physical Science and Technology, Xiamen University, Xiamen 361005, China*<sup>3</sup>*Chongqing Key Laboratory of Precision Optics, Chongqing Institute of East China Normal University, Chongqing 401121, China*<sup>4</sup>*Collaborative Innovation Center of Extreme Optics, Shanxi University, Taiyuan, Shanxi 030006, China*<sup>5</sup>*CAS Center for Excellence in Ultra-intense Laser Science, Shanghai 201800, China*

(Received 12 October 2022; revised 27 January 2023; accepted 30 January 2023; published 10 February 2023)

Parametric scattering dynamics are general and of crucial importance for cavity exciton polaritons. Here, parametric scattering process driven by exciton polariton condensates has been revealed in a 1D ZnO microcavity between the whispering-gallery mode and quasiwhispering-gallery mode. When the occupation of the produced polariton condensate is dense enough, polariton condensates formed on quasiwhispering-gallery mode can be scattered towards the ground state of the adjacent whispering-gallery modes at higher and lower energies. By using the femtosecond angle-resolved spectroscopic imaging technique, the ultrafast dynamics of this intermode polariton parametric scattering have been explicitly observed. The scattering towards a higher mode occurs faster than that to a lower-energy mode by less than a picosecond. The revealed dynamics can not only expand the present investigations on polariton parametric scattering, but also promote the potential applications in, e.g., quantum information processing.

DOI: [10.1103/PhysRevB.107.L060303](https://doi.org/10.1103/PhysRevB.107.L060303)

Cavity exciton polaritons (EPs) are part-light, part-matter bosonic quasiparticles generated from the strong coupling between excitons and confined cavity photons [1]. The photonic nature provides EPs with extremely light effective mass ( $\sim 10^{-5}$ – $10^{-4} m_e$ , where  $m_e$  is the mass of an electron) [2], which is regarded as a crucial factor for the realization of Bose-Einstein condensation at high temperatures [3]. That is, when the interparticle distances decrease to the level of their de Broglie wavelengths, polaritons will dramatically accumulate, resulting in a stimulated condensation. In addition, strong interactions among polaritonic ensemble inherited from the excitonic constituents bring about high nonlinearity. Rapid development in the related fields has resulted in the emergence of polaritonic devices involving amplifiers [4], switches [5], transistors [6], and so on.

Among the unique polaritonic characteristics, the polariton parametric scattering (PPS) has been widely explored in the past decades. On the one hand, PPS is of fundamental importance since it is responsible for the formation and the intrinsic properties of polaritons [7–10]. Parametric oscillation [11], interbranch PPS [9,10,12,13], and polarization-inversion PPS [14] have been experimentally observed. On the other hand, PPS provides unique potential for advanced applications. For instance, interbranch PPS can be driven by polariton condensates in multibranch cavity systems. The degenerated

scattered pairs are intrinsically entangled, and thus can serve as ideal candidates for quantum information processing [9]. Compared with photons which can be made entangled, polaritons possess stronger nonlinearity inherited from their excitonic constituent, and thus can be regulated more efficiently. For example, quantum bits can be produced based on EPs, providing effective interfaces between nodes and channels in distributed quantum networks [15,16].

As compared to the polariton condensates formed at cryogenic temperatures [17,18], room-temperature polaritons in the microcavity systems based on GaN [19], ZnO [7], perovskite [20], and organic materials [21,22] have been realized, which are desired for the real-life applications. Among them, the ZnO-based microcavity has attracted much attention due to its well-developed fabrication and multibranch behavior in its 1D microcavity. In the ZnO microwire with hexagonal cross sections, three kinds of optical modes can be formed, namely whispering-gallery mode (WGM), quasiwhispering-gallery mode (q-WGM), and Fabry-Perot mode (FPM) [as shown in the insets of Fig. 1(a)]. When the radius of the microwire is small, the optimized mode is WGM. When the radius is large, in order to reduce the loss in the medium, FPM with the shortest optical path tends to dominate. For the sizes in between, WGMs and q-WGMs may coexist in the system [23–25]. In this paper, intermode parametric scattering of EP condensates between WGM and q-WGM has been visualized with femtosecond resolution in the ZnO microwire at room temperature. EPs are excited nonresonantly using femtosecond laser pulses and the condensation on the ground states on various lower polariton (LP) branches can be generated. By using the femtosecond angle-resolved spectroscopic imaging

\*These authors contributed equally to this work.

†hli@lps.ecnu.edu.cn

‡zhanghai@xmu.edu.cn

§jwu@phy.ecnu.edu.cn

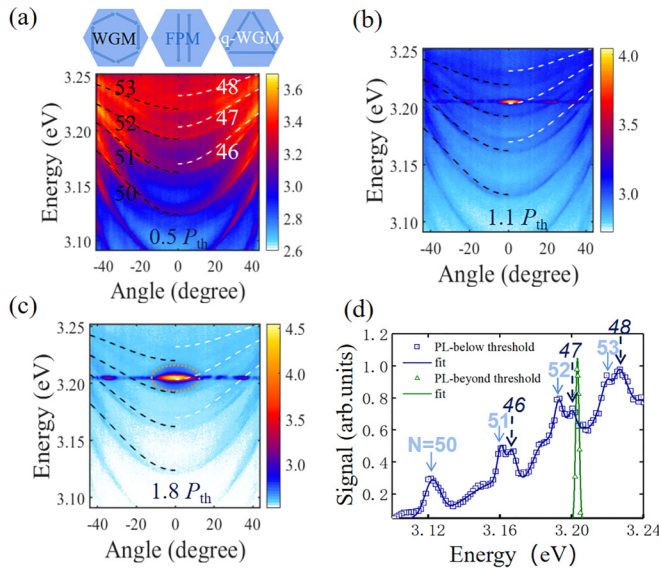


FIG. 1. Steady-state angle-resolved PL spectra obtained at the pump fluences of (a)  $0.5 P_{th}$ , (b)  $1.1 P_{th}$ , and (c)  $1.8 P_{th}$ . Here,  $P_{th}$  represents the condensation threshold. The black and white dashed curves are the fitted dispersion curves for the WGMs and the q-WGMs, respectively. The inset figures on the top of (a) are the schematic drawings of the three optical modes in the ZnO microcavity, namely the WGM, FPM, and q-WGM, respectively. (d) Angle-integrated spectra of the PL emission around  $k_{||} = 0$  at the excitation fluence below (blue data) and beyond (green data) the condensation threshold. The solid line is obtained by Gaussian multimodal fitting. Ground states of WGM (q-WGM) with different  $N$  are marked by the solid (dashed) arrows.

(FARSI) technique [13,26], the angle-resolved energy spectra of the photoluminescence (PL) emission of EP condensates is recorded with femtosecond resolution, where the intermode PPS has been unambiguously visualized. When the density of condensates reaches a certain level, we found that the condensates start scattering from q-WGMs to the ground states of the adjacent WGMs, generating transient condensation population lasting for a few picoseconds.

Experimentally, the ZnO microwires are grown along the  $c$  axis by the chemical vapor deposition method. Femtosecond laser pulses (800 nm, 35 fs, 1 kHz) delivered from a Ti:sapphire amplification system are sent to an optical parametric amplifier, from which the excitation pulses at the central wavelength of 350 nm with the duration of about 70 fs are generated. These pulses are guided and focused onto the ZnO microcavity through a  $15\times$  objective, resulting in a focusing spot of  $\sim 4 \mu\text{m}$  in diameter. The  $k$ -space PL emission of the EP condensates is detected by a spectrometer equipped with a two-dimensional intensified charge-coupled detector. The polaritonic properties are investigated by the angle-resolved PL spectroscopy. The FARSI technique is utilized to obtain the PL distributions with femtosecond resolution in both the energy and the momentum degrees of freedom with femtosecond time resolution based on the transient Kerr effect [8,13,26–28]. All the measurements are applied on the transverse electronic (TE) polarization.

The steady-state dispersion mapping obtained below condensation threshold is shown in Fig. 1(a). Two series of

parabolic-like dispersion with different curvatures (obtained by fitting with the plane-wave model [29]) can be recognized. They are marked by the black (WGM) and the white (q-WGM) dashed curves, respectively. In general, the WGM and q-WGM in ZnO microwires can be distinguished by their quality ( $Q$ ) factors [30,31]. The WGMs generally exhibit higher  $Q$  factors ( $Q \sim 1500$ ) compared with those for the q-WGMs ( $Q \sim 500$ ) in the same sample. As the pump fluence increases, upon reaching the condensation threshold, the PL distribution near  $\theta = 0^\circ$  (equivalent to  $k_{||} = 0$ ) shows a sharp increase of the emission intensity, as shown in Figs. 1(b) and 1(c). Early work demonstrated that the detuning ( $\delta = E_{\text{photon}} - E_{\text{exciton}}$ ) could serve as a crucial parameter to determine the threshold of exciton polariton condensation [30,32]. The competition of kinetics and thermodynamics mechanisms usually results in the build-up of EP condensates at a positive optimal detuning in ZnO microwires operated at room temperature [33]. Accordingly, the EP condensates are preferentially formed on the ground state of a q-WGM ( $N = 47$ ) due to the fact that the detuning in this specific mode ( $\sim 177$  meV) is at the optimum regime. The energy blueshift of the condensate around  $k_{||} = 0$  ( $\sim 2.5$  meV) can be extracted in Figs. 1(b) and 1(c), which can be more clearly seen in the angle-integrated spectra shown in Fig. 1(d). Interestingly, we noticed that a “halo” surrounding the condensate [labeled with an orange dashed circle in Fig. 1(c)] shows up at the pump fluence of  $\sim 1.8 P_{th}$ , where  $P_{th} \sim 5.0 \text{ mJ/cm}^2$  represents the threshold excitation fluence of the condensation in the present study.

By using the FARSI technique, the angle-resolved PL spectra are measured with subpicosecond resolution. As we integrate on the momentum degree of freedom, the derived EP condensate distributions as a function of energy and time for various pump fluences can be obtained and are presented in Figs. 2(a)–2(c). The formation dynamics of the halo discovered in steady-state measurement [shown in Fig. 1(c)] can be revealed by these time-resolved observations. For instance, the condensate emerges at an energy of  $\sim 3.207$  eV on a q-WGM ( $N = 47$ ), and the signals parametrically scattered towards the higher and lower energies populating on the ground states of the WGMs with  $N = 53$  and 52 (as indicated by the black arrows). The energy of the scattered signals, which are in the same momentum regime of their scattering sources [shown in the inset figure in Fig. 2(d)], satisfy  $E_{\text{WGM}-53} + E_{\text{WGM}-52} = 2E_{\text{qWGM}-47}$ . These processes, fulfilling the conservation of energy and momentum, can be attributed to the PPS between the q-WGM and the WGM. In addition, ultrashort duration of the scattered signals can be identified, e.g.,  $\sim 2.2$  ps for the data shown in Fig. 2(a). The short lifetime combining with the weak intensity of the scattered signals attribute to the halo obtained in the steady-state measurement. As shown in Figs. 2(a)–2(c), the dynamical redshift of the EP condensates can be observed for each scan (as being indicated by the white dashed curves), corresponding to the gradual reduction of the condensate density [13,34]. The stronger pump fluence can produce a higher EP density, therefore resulting in an increase of the nonlinear interactions among polaritons. This will bring an energy blueshift of the initially formed condensates (where the condensates emerge at about 3.207, 3.209, and 3.213 eV as we increase

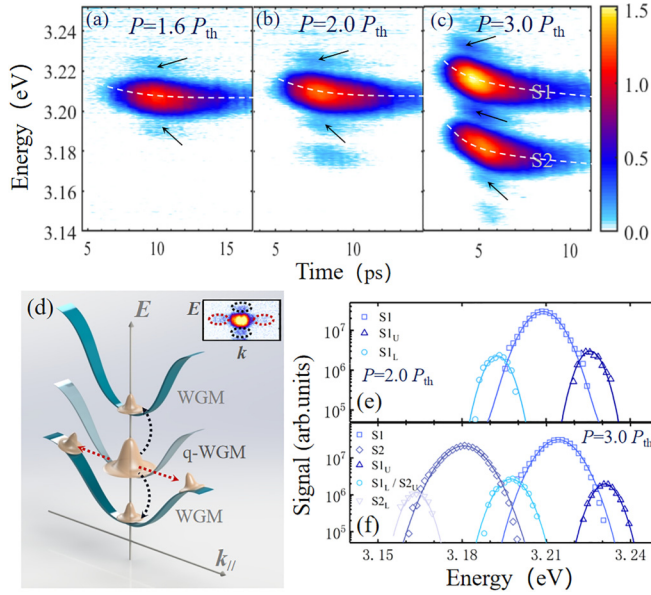


FIG. 2. Dynamics of the intermode PPS. (a)–(c) PL distributions (integrated around  $k_{||} = 0$ ) as a function of time and energy obtained at different pump fluences: (a)  $1.6 P_{th}$ , (b)  $2.0 P_{th}$ , and (c)  $3.0 P_{th}$ . Black arrows indicate the scattered signals. White dashed curve of the time-dependent redshift helps to guide the eyes. (d) Schematic diagrams of the intermode PPS (indicated by the black dashed arrows) and degenerate PPS (indicated by the red dashed arrows). The inset figure shows an instantaneous angle-resolved PL spectra obtained from FARSI measurement. The extracted scattered signals and their scattering sources obtained at (e)  $P = 2.0 P_{th}$  and (f)  $P = 3.0 P_{th}$ . Solid curves are fitting results with Gaussian function.

the pump fluence) accompanying with a faster redshift afterwards. Meanwhile, the scattered signals towards the upper and lower directions in the energy degree of freedom show similar pump-fluence dependent characteristics compared with their scattering source.

A schematic diagram of the intermode PPS process is illustrated in Fig. 2(d). The scattering source of the polariton condensates is initially formed on the ground state of a q-WGM. Parametric scattering can take place towards the adjacent LP branches in a degenerate manner (indicated by the red dashed arrows) or to different energy levels maintaining the same momentum (indicated by the black dashed arrows). The whole process is governed by the conservation of energy and momentum. As a matter of fact, these two kinds of scattering signals can both be clearly recognized in the time- and angle-resolved PL spectra in the FARSI measurement, as presented in the inset figure in Fig. 2(d). The populations of the scattering signals in the upper and lower energies as well as their sources are extracted for the measurements obtained at  $P = 2.0 P_{th}$  and  $3.0 P_{th}$  as being presented in Figs. 2(e) and 2(f), respectively. The energy differences of  $S1_U$  and  $S1_L$  (representing the scattering signal to the upper and lower branches from  $S1$ ) with respect to their scattering source  $S1$  are identical ( $\Delta E = 17$  meV). When the pump fluence increases from  $2.0 P_{th}$  to  $3.0 P_{th}$ , the energy of  $S1$  has an overall blueshift of about 5 meV, while  $\Delta E$  remains the same. Moreover, a new condensate appears on the lower energy [13] of about 3.18 eV (q-WGM,  $N = 46$ ) which has been marked by  $S2$  in Fig. 2(c).

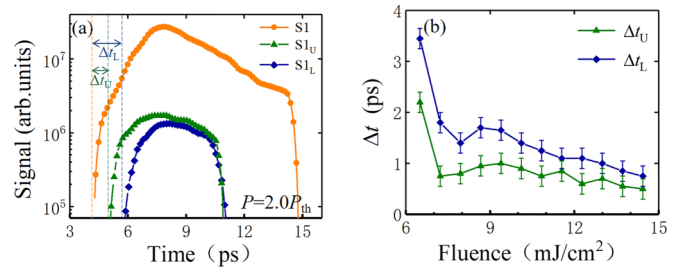


FIG. 3. (a) Time-resolved signal of  $S1$ ,  $S1_U$ , and  $S1_L$  at  $P = 2.0 P_{th}$  (in log scale). (b) Excitation fluence-dependent measurement of  $\Delta t_U$  and  $\Delta t_L$ .  $\Delta t_U$  ( $\Delta t_L$ ) is the scattering time to  $S1_U$  ( $S1_L$ ).

Here, the injected density of the EP condensate of  $S2$  exceeds the scattering threshold, resulting in an extra intermode PPS process. In the time-integrated spectra shown in Fig. 2(f), we find that the signal of  $S1_L/S2_U$  equals to the sum of  $S1_U$  and  $S2_L$ . The  $S1_L$  and  $S2_U$  signals are degenerate; they occupy the same WGM of  $N = 52$ .

The dynamics of this intermode parametric scattering process can be further revealed by the femtosecond-resolved measurements. The time-resolved signals for  $P = 2.0 P_{th}$  are shown in Fig. 3(a). From this we can see that the occurrence time of the signals of  $S1$ ,  $S1_U$ , and  $S1_L$  are at about 4.28, 5.16, and 5.88 ps, respectively. A general trend is that the scattering source appears first, followed by the scattered signal toward the upper-energy level, and the lower-energy signal comes later. A systematic measurement of the scattering time to the upper and lower energies (denoted as  $\Delta t_U$  and  $\Delta t_L$ ) is performed for a series of pump fluences. With the increased fluence,  $\Delta t_U$  and  $\Delta t_L$  are both decreasing to less than 1 ps and the difference between them is at hundreds of femtosecond. This also corresponds to a rising of the scattering rate. The pump-fluence dependent measurement also shows that  $\Delta t_U$  is always smaller than  $\Delta t_L$ . The polaritonic wave function scattered upward has a larger overlap with the reservoir compared with the polaritons scattered to the lower branch [35]. The higher-energy mode in general exhibits more excitonic components, thus possessing stronger nonlinearity. It is preferred to be populated by the scattered particles. This could be the reason for the earlier population of EPs on the upper-scattered energy level. As a result, although the scattering EP pair is generated simultaneously, the observed upper- and lower-scattering signals do not appear simultaneously.

A theoretical model based on polariton-polariton intermode scattering in a multimode cavity is utilized to understand the experimental observations. In this model, conservation of energy and momentum are fulfilled ( $\tilde{E}_{LP}^{(i)}(k+q) + \tilde{E}_{LP}^{(j)}(k-q) - 2\tilde{E}_{LP}^{(l)}(k) = 0$ , where  $i, j, l$  represent different LP branches). The amplitude of polariton wave function  $\psi_i(k)$  can be numerically solved by using the following equation [36,37]:

$$\begin{aligned} i\hbar \frac{d\psi_i(k)}{dt} = & [\tilde{E}_{LP}^i(k) + i(R_i F_0(k) - \gamma_i)] \psi_i(k) \\ & + \sum_{j,l} \sum_q [2E_i^{ijl} P_i^*(k) P_j(k+q) P_l(k-q) \\ & + E_i^{ijl} P_j^*(k-2q) P_l^*(k-q)]. \end{aligned}$$

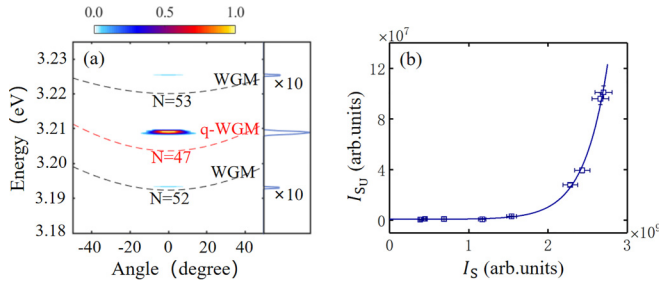


FIG. 4. Calculation results of the intermode polariton condensate scattering between WGM and q-WGM. (a) Calculated steady-state angle-resolved PL distribution. (b) Theoretical fitting of the scattering process. Scattered hollow squares represent the dependence of the scattered signal  $I_{S_U}$  on the scattering source  $I_S$ . The Solid curve is the fitting results using rate equations.

The energy blueshifts can be written as  $\tilde{E}_{LP}^{(i)}(k) = E_{LP}^{(i)}(k) + 2V_{k,k,0}^{ijl}|P_{k,j}|^2$ .  $|P_{k,j}|^2$  represents the occupation of polariton with wave vector  $k$  in mode  $j$ . The coupling energy is  $E_i^{ijl}(k) = \frac{1}{2}(V_{k,k,q}^{ijl} + V_{k,k,-q}^{ijl})$ , and the effective potential  $V_{k,k',q}^{hij} = g_0 X_{k+q,i} X_{k'-q,j} X_{k,l} X_{k',l}$  is induced by the exciton-exciton interaction, where  $X$  is the excitonic fraction of the corresponding LP branch which can be obtained from the coupled oscillator model, and  $g_0$  is the coupling factor. In addition,  $R_i$  represents the scattering rate from the exciton reservoir to the LP branches.  $F_0$  is the exciton reservoir and  $\gamma_i$  is the decay rate which can be extracted from the excitonic and photonic fraction of the LPs [2].

Calculation results of the steady-state angle-resolved PL distribution are shown in Fig. 4(a). The calculated occupation energies are in quantitative agreement with our observations. The scattering source of polariton condensate populates on the q-WGM with  $N = 47$ , exhibiting a blueshift due to the strong interaction among polaritons. The scattered signals populate

on the WGMs with  $N = 53$  and  $52$ . However, restricted by the calculation capability, approximations in the time degree of freedom have been applied in the present model. The results thus cannot agree with our experimental results regarding the dynamics. We further investigate the dependence of the intensity of the scattered signal (noted as  $I_{S_U}$ ) with respect to their sources ( $I_S$ ). The results are shown in Fig. 4(b). The solid line in the figure is a fitting result obtained from rate equations [9]. A clear threshold behavior can be recognized, presenting the characteristics of PPS. In addition, the polariton density can be extracted from this calculation. It is estimated to be  $\sim 10^{17} \text{ cm}^{-3}$  at the threshold, which is two orders of magnitude smaller than the Mott density ( $\sim 10^{19} \text{ cm}^{-3}$ ) for the ZnO system [38]. This could guarantee that the studied processes are in the strong-coupling regime.

In conclusion, by using the FARSI technique, the ultrafast dynamics of intermode PPS from q-WGM to WGM have been revealed in a 1D ZnO microcavity. The scattering towards adjacent branches at higher and lower energies can be distinguished with subpicosecond resolutions. Pump-fluence dependent measurements show that the scattered signal observed in the upper-energy level always show up earlier by hundreds of femtoseconds compared to those being obtained in the lower-energy level. Combining with the calculation results from a multimode parametric scattering model, the specific scattering channels have been identified. Our results not only enrich the study of polariton parametric scattering but also provide inspirations for polaritonic quantum applications.

This work is supported by the National Key R&D Program of China (Grants No. 2018YFA0306303 and No. 2018YFA0306304); the National Natural Science Fund (Grants No. 92050105, No. 92250301, No. 12241407, No. 12227807, No. 91950201, and No.11834004); the project is supported by the Shanghai Committee of Science and Technology, China (Grants No. 22ZR1419700 and No. 19ZR1473900).

- [1] C. Weisbuch, M. Nishioka, A. Ishikawa, and Y. Arakawa, *Phys. Rev. Lett.* **69**, 3314 (1992).
- [2] H. Deng, H. Haug, and Y. Yamamoto, *Rev. Mod. Phys.* **82**, 1489 (2010).
- [3] T. Byrnes, N. Y. Kim, and Y. Yamamoto, *Nat. Phys.* **10**, 803 (2014).
- [4] P. G. Savvidis, J. J. Baumberg, R. M. Stevenson, M. S. Skolnick, D. M. Whittaker, and J. S. Roberts, *Phys. Rev. Lett.* **84**, 1547 (2000).
- [5] T. Gao, P. S. Eldridge, T. C. H. Liew, S. I. Tsintzos, G. Stavrinidis, G. Deligeorgis, Z. Hatzopoulos, and P. G. Savvidis, *Phys. Rev. B* **85**, 235102 (2012).
- [6] D. Ballarini, M. De Giorgi, E. Cancellieri, R. Houdre, E. Giacobino, R. Cingolani, A. Bramati, G. Gigli, and D. Sanvitto, *Nat. Commun.* **4**, 1778 (2013).
- [7] L. Sun, Z. Chen, Q. Ren, K. Yu, L. Bai, W. Zhou, H. Xiong, Z. Q. Zhu, and X. Shen, *Phys. Rev. Lett.* **100**, 156403 (2008).
- [8] F. Chen, H. Zhou, Z. Ye, S. Luo, Z. Sun, Y. Zheng, X. Chen, H. Xu, H. Xu, T. Byrnes *et al.*, *Phys. Rev. B* **106**, L020301 (2022).
- [9] W. Xie, H. Dong, S. Zhang, L. Sun, W. Zhou, Y. Ling, J. Lu, X. Shen, and Z. Chen, *Phys. Rev. Lett.* **108**, 166401 (2012).
- [10] J. Wu, S. Ghosh, R. Su, A. Fieramosca, T. C. H. Liew, and Q. Xiong, *Nano Lett.* **21**, 3120 (2021).
- [11] C. Diederichs, J. Tignon, G. Dasbach, C. Ciuti, A. Lemaitre, J. Bloch, P. Roussignol, and C. Delalande, *Nature (London)* **440**, 904 (2006).
- [12] G. Dasbach, M. Schwab, M. Bayer, D. N. Krizhanovskii, and A. Forchel, *Phys. Rev. B* **66**, 201201(R) (2002).
- [13] F. Chen, H. Zhou, H. Li, J. Cao, S. Luo, Z. Sun, Z. Zhang, Z. Shao, F. Sun, B. Zhou *et al.*, *Nano Lett.* **22**, 2023 (2022).
- [14] G. Dasbach, C. Diederichs, J. Tignon, C. Ciuti, P. Roussignol, C. Delalande, M. Bayer, and A. Forchel, *Phys. Rev. B* **71**, 161308(R) (2005).
- [15] A. Reiserer and G. Rempe, *Rev. Mod. Phys.* **87**, 1379 (2015).
- [16] A. Cuevas, J. C. Lopez Carreno, B. Silva, M. De Giorgi, D. G. Suarez-Forero, C. S. Munoz, A. Fieramosca, F. Cardano, L. Marrucci, V. Tasco *et al.*, *Sci. Adv.* **4**, eaao6814 (2018).

- [17] J. Kasprzak, M. Richard, S. Kundermann, A. Baas, P. Jeambrun, J. M. Keeling, F. M. Marchetti, M. H. Szymanska, R. Andre, J. L. Staehli *et al.*, *Nature (London)* **443**, 409 (2006).
- [18] R. Balili, V. Hartwell, D. Snoke, L. Pfeiffer, and K. West, *Science* **316**, 1007 (2007).
- [19] S. Christopoulos, G. Baldassarri Hoger von Hogersthal, A. Grundy, P. G. Lagoudakis, A. V. Kavokin, J. J. Baumberg, G. Christmann, R. Butte, E. Feltin, J. F. Carlin *et al.*, *Phys. Rev. Lett.* **98**, 126405 (2007).
- [20] R. Su, C. Diederichs, J. Wang, T. C. H. Liew, J. Zhao, S. Liu, W. Xu, Z. Chen, and Q. Xiong, *Nano Lett.* **17**, 3982 (2017).
- [21] S. Kena-Cohen and S. R. Forrest, *Nat. Photonics* **4**, 371 (2010).
- [22] K. S. Daskalakis, S. A. Maier, R. Murray, and S. Kena-Cohen, *Nat. Mater.* **13**, 272 (2014).
- [23] M. Grundmann and C. P. Dietrich, *Phys. Status Solidi B* **249**, 871 (2012).
- [24] K. Qiu, Y. Zhao, Y. Gao, X. Liu, X. Ji, S. Cao, J. Tang, Y. Sun, D. Zhang, B. Feng *et al.*, *Appl. Phys. Lett.* **104**, 081109 (2014).
- [25] G. P. Zhu, C. X. Xu, J. Zhu, C. G. Lv, and Y. P. Cui, *Appl. Phys. Lett.* **94**, 051106 (2009).
- [26] F. Chen, H. Li, H. Zhou, Z. Ye, S. Luo, Z. Sun, F. Sun, J. Wang, H. Xu, H. Xu *et al.*, *J. Phys.: Condens. Matter* **34**, 024001 (2021).
- [27] Z. Ye, F. Chen, H. Zhou, S. Luo, F. Sun, Z. Sun, Y. Zheng, X. Chen, H. Xu, Z. Chen *et al.*, *J. Phys.: Condens. Matter* **34**, 22LT01 (2022).
- [28] F. Chen, H. Li, H. Zhou, S. Luo, Z. Sun, Z. Ye, F. Sun, J. Wang, Y. Zheng, X. Chen *et al.*, *Phys. Rev. Lett.* **129**, 057402 (2022).
- [29] T. Nobis, E. M. Kaidashev, A. Rahm, M. Lorenz, and M. Grundmann, *Phys. Rev. Lett.* **93**, 103903 (2004).
- [30] Q. Duan, D. Xu, W. Liu, J. Lu, L. Zhang, J. Wang, Y. Wang, J. Gu, T. Hu, W. Xie *et al.*, *Appl. Phys. Lett.* **103**, 022103 (2013).
- [31] L. Sun, H. Dong, W. Xie, Z. An, X. Shen, and Z. Chen, *Opt. Express* **18**, 15371 (2010).
- [32] S. Luo, Y. Wang, L. Liao, Z. Zhang, X. Shen, and Z. Chen, *J. Appl. Phys.* **127**, 025702 (2020).
- [33] D. Xu, W. Xie, W. Liu, J. Wang, L. Zhang, Y. Wang, S. Zhang, L. Sun, X. Shen, and Z. Chen, *Appl. Phys. Lett.* **104**, 082101 (2014).
- [34] M. De Giorgi, D. Ballarini, P. Cazzato, G. Deligeorgis, S. I. Tsintzos, Z. Hatzopoulos, P. G. Savvidis, G. Gigli, F. P. Laussy, and D. Sanvitto, *Phys. Rev. Lett.* **112**, 113602 (2014).
- [35] A. Askitopoulos, T. C. H. Liew, H. Ohadi, Z. Hatzopoulos, P. G. Savvidis, and P. G. Lagoudakis, *Phys. Rev. B* **92**, 035305 (2015).
- [36] C. P. Dietrich, R. Johne, T. Michalsky, C. Sturm, P. Eastham, H. Franke, M. Lange, M. Grundmann, and R. Schmidt-Grund, *Phys. Rev. B* **91**, 041202(R) (2015).
- [37] C. Ciuti, P. Schwendimann, B. Deveaud, and A. Quattropani, *Phys. Rev. B* **62**, R4825 (2000).
- [38] L. Zhang, W. Xie, J. Wang, A. Poddubny, J. Lu, Y. Wang, J. Gu, W. Liu, D. Xu, X. Shen *et al.*, *Proc. Nat. Acad. Sci. USA* **112**, E1516 (2015).